



Study of Structural, Dielectric, Electrical, and Magnetic Properties of Samarium-Doped Double Perovskite Material for Thermistor Applications

Priyambada Mallick¹ · Santosh Ku. Satpathy¹ · Banarji Behera²

Received: 10 March 2022 / Accepted: 25 August 2022 / Published online: 5 September 2022
© The Author(s) under exclusive licence to Sociedade Brasileira de Física 2022, corrected publication 2022

Abstract

0.5(BiSm_yFe_{1-y}O₃)-0.5(PbZrO₃) ($y=0.05, 0.10, 0.15, \text{ and } 0.20$) ceramics are synthesized through solid-state reaction technique. Room temperature X-Ray diffraction technique is used for analyzing the structural information. The scanning electron microscope reveals the homogeneous distribution of grains. The dielectric constant and loss tangent increase as the temperature rises. Low remanent polarization indicates the weak nature of ferroelectricity. The Nyquist plot confirms the contribution of bulk effect in the materials. The activation energies are calculated from the conductivity curve using least square fitting. The spectrum of ac conductivity followed the universal Johnson power law. A low remanent magnetization is found from the M-H curve. Thermistor constant (β), sensitivity factor (α), and stability factor for all the samples are calculated which confirms the characteristics of the NTC thermistor.

Keywords Solid-state reaction · X-ray diffraction · Impedance · Electrical conductivity · Magnetic properties · Thermistor constant

1 Introduction

Bismuth ferrite (BiFeO₃) is one of the essential multiferroic materials in recent days [1]. The novelty of the BiFeO₃ (BFO) shows both ferroelectric and ferromagnetic behavior. It also has the G-type spin configuration in its pseudo-cubic rhombohedral structure [2]. Due to the strong absorption band of BiFeO₃ in the ultraviolet light region and weak absorption band in the visible light region, it has various applications such as spintronic, photovoltaics, non-volatile logic, and multi-state memory devices [1, 3–8]. BiFeO₃

exhibits some secondary phases for which significant issues in industrial fields like large leakage current, high impurity phases, and losses in dielectric properties generate [9–13]. Bismuth ferrite-based single-phase multiferroic generally have weak macroscopic magnetic properties [14, 15]. Partially doping rare earth metals with BiFeO₃-based material helps in improving electric, magnetic, optical, and dielectric properties (increase dielectric constant, reduce optical band gap and dielectric loss, etc.), which needs to create a new type of functional materials for various applications [16, 17]. The doping of rare earth ion provides a wonderful opportunity to regulate the physical characteristics of BiFeO₃-based material by eliminating the impurity phase in BFO. As a result, it is subject of studies in rare earth-doped BFO-based materials. In this report, rare-earth metal samarium (Sm) was partially substituted at the bismuth site of BiFeO₃-PbZrO₃ [17]. In lead zirconate titanate (PZT), doping of samarium (Sm³⁺) helps to raise the ferroelectricity behavior, dielectric constant, and decrease the dielectric loss which is very helpful for ferroelectric memory and sensing/actuating applications [18]. Samarium also helps to enhance the electrical permittivity, AC conductivity, and remanent magnetization of BFO [19–21] which can be applied for energy storage devices, and PV cells. Few works have been done on the

✉ Santosh Ku. Satpathy
santosh.satpathy@cutm.ac.in

Priyambada Mallick
priyambadamallick17@gmail.com

Banarji Behera
banarjibehera@gmail.com

¹ Centurion University of Technology and Management,
Bhubaneswar, Odisha, India

² Materials Research Laboratory, School of Physics,
Sambalpur University, Jyoti Vihar, Burla 768019, Odisha,
India

properties of BiFeO₃-PbZrO₃ for the last few years due to the antiferroelectric characteristics of lead zirconate (PZO), which helps in developing energy storage devices [22]. Our group has also reported BiFeO₃-PbZrO₃ [23–27]. In this paper, structural, dielectric, microstructural, electrical, ferroelectric, and magnetic properties of Sm-doped double perovskite BiFeO₃-PbZrO₃ for thermistor applications.

2 Experimental Procedure

0.5(BiSm_yFe_{1-y}O₃)-0.5(PbZrO₃) ($y = 0.05, 0.10, 0.15, \text{ and } 0.20$) ceramics are prepared in an appropriate stoichiometry with ingredients, i.e., bismuth oxide (M/s. Spectrochem Pvt. Ltd., with purity > 99.9%), ferric oxide (M/s. Blulux with purity > 98.5%), samarium oxide (M/s. Spectrochem Pvt. Ltd., with purity > 99.9%), lead oxide (M/s. Blulux with purity 98.5%), and zirconium oxide (M/s. Sigma-Aldrich with purity > 99.9%) by solid-state reaction technique as given in Table 1. The oxides have been carefully mixed and blended by using an agate mortar and pestle for 2 h in an air atmosphere and then 1 h in methanol. The mixed powders are calcined at an optimized temperature of 800 °C for 5 h. Using a hydraulic press, the calcinated powder turned into 10-mm diameter and 1–2-mm-thick cylindrical pellets by cold pressing at a pressure of $3.5 \times 10^6 \text{ N/m}^2$. Polyvinyl alcohol (PVA) has been taken as a binder to decrease the pellets' brittleness that burned out during sintering. Then, the pellets are sintered at 850 °C for 6 h. The formation of the materials and quality are studied using the X-ray powder diffraction (Rigaku Miniflex, Japan) technique using CuK α radiation where the wavelength (λ) of radiation is 1.5405 Å at a broad range of Bragg angle 2θ ($20^\circ \leq 2\theta \leq 80^\circ$), scanning speed of 3°/min at room temperature. Both sides of sintered pellets are electrodes with air-drying silver paste to investigate the electrical characteristics of the materials. To remove the remaining moisture, the pellets are dried for 4 h at 150 °C after electroding and then cooled to room temperature. Impedance measurements are performed in the

Table 1 Stoichiometric amount of 0.5 (BiSm_yFe_{1-y}O₃)-0.5(PbZrO₃) ($y = 0.05, 0.10, 0.15, 0.20$)

| Ingredients (gm) | 0.5 (BiSm _y Fe _{1-y} O ₃)-0.5(PbZrO ₃) | | | |
|--------------------------------|--|------------|------------|------------|
| | $y = 0.05$ | $y = 0.10$ | $y = 0.15$ | $y = 0.20$ |
| Bi ₂ O ₃ | 4.5814 | 4.3667 | 4.1495 | 3.9295 |
| Fe ₂ O ₃ | 1.6527 | 1.6628 | 1.6730 | 1.6834 |
| Sm ₂ O ₃ | 0.1804 | 0.3631 | 0.5480 | 0.7352 |
| Pb ₂ O ₃ | 2.3105 | 2.3242 | 2.3384 | 2.3529 |
| ZrCo ₂ | 1.2750 | 1.2832 | 0.1291 | 1.2990 |

frequency range of 10^2 – 10^6 Hz from 25 to 450 °C using an LCR meter (HIOKI Model 3532). The micrographs at different magnifications are taken using JEOL JSM-5800 Scanning Electron Microscope. An automatic PE loop tracer is used for the characterization of materials for ferroelectric properties. The magnetic properties are studied by vibrating-sample magnetometer (Lakeshore-7404).

3 Results and Discussion

3.1 Structural Properties

Figure 1(a, b) shows the X-ray diffraction pattern and impurity phase of 0.5(BiFe_ySm_{1-y}O₃)-0.5(PbZrO₃) ($y = 0.05, 0.10, 0.15, 0.20$). All the diffraction peaks are indexed and in good agreement with unit cell parameters for the rhombohedral structure of Space group R3c. Diffraction peak (200) at 32° is indexed to higher 2θ angles and became a narrow and single peak with a rising amount of dopant samarium in the samples (Fig. 1(a)). This variation arises due to phase impurities such as Bi₂₄Fe₄₀, Bi₂Fe₄O₉, and Sm₂O₃ as they are thermodynamically stable [23] at high temperatures, which is shown in Fig. 1(b). The size of crystallite (P) is estimated practically from the broadening of XRD peaks using Scherrer's equation [28] $P = \frac{K\lambda}{\beta_{1/2} \cos \theta_{br}}$, where $K = \text{shape constant} = 0.89$, $\lambda = 1.5405 \text{ \AA}$, and $\beta_{1/2} = \text{peak width of the reflection at half intensity}$. The average value of the size of the crystallite is between 16 and 18 nm.

Higher percent crystallinity of the samples indicates a high melting point, i.e., more hardness of the material, and also enhances mechanical strength, opacity, and thermal properties which were calculated from XRD by using the relation

$$\text{Crystallinity} = \frac{\text{Area of the crystalline peaks}}{\text{Area of (Crystalline + Amorphous) all the peaks}} \times 100$$

The dislocation density and micro-strain of all the samples were observed to be inversely interdependent with the crystallite size (given in Table 2). This variation confirmed the smaller number of lattice defects in the materials due to the decrease in the availability of grain boundaries with a rise in crystallite size.

3.2 Microstructural Properties

SEM micrograph of 0.5(BiSm_yFe_{1-y}O₃)-0.5(PbZrO₃) ($y = 0.05, 0.10, 0.15, 0.20$) is shown in Fig. 2. The grains are spread homogeneously across the material's entire surface. The nature of the microstructure stated that the grains are spherical and tightly packed in the materials. The grain shape observed in these micrographs is polycrystalline and

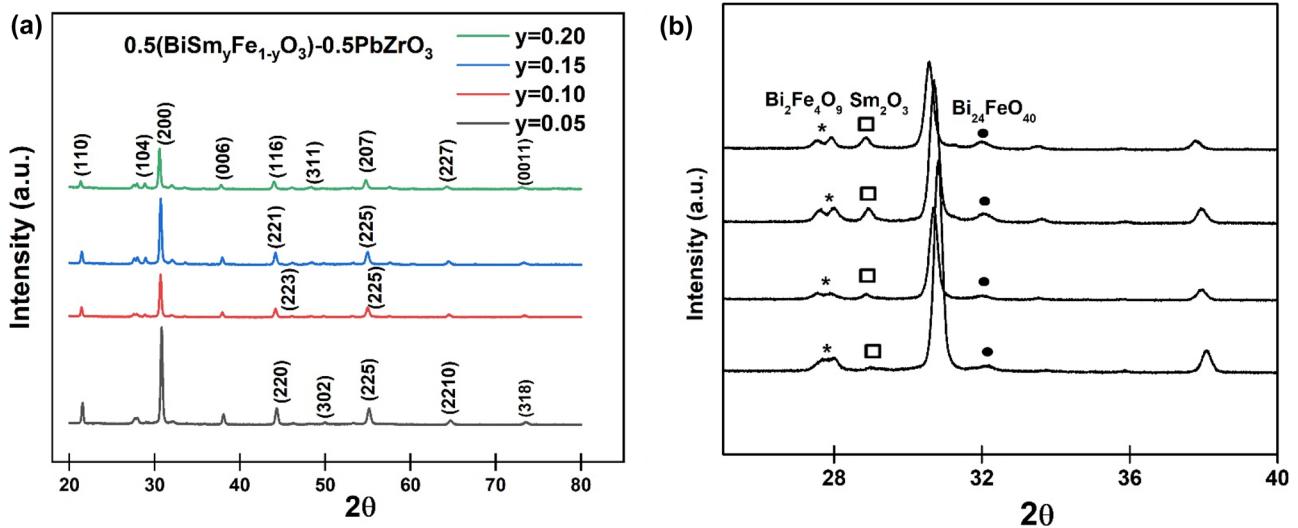


Fig. 1 (a) X-ray diffraction pattern and (b) impurities phase of $0.5(\text{BiSm}_y\text{Fe}_{1-y}\text{O}_3)-0.5(\text{PbZrO}_3)$ ($y=0.05, 0.10, 0.15, 0.20$)

the average grain sizes are found to be within the 5- μm range in the materials. The grain sizes are more significant than the estimated crystallite size of the materials.

3.3 Dielectric Study

The dielectric constant (ϵ_r) and tangent loss ($\tan\delta$) of $0.5(\text{BiSm}_y\text{Fe}_{1-y}\text{O}_3)-0.5(\text{PbZrO}_3)$ taking $y=0.05, 0.10, 0.15, 0.20$ as a function of temperature at 500kHz is shown in Fig. 3. The dielectric anomaly was observed for all the materials, which is shown in Table 3. The value of the dielectric constant rises with increasing temperature and attains maximum value at the transition temperature. These transition temperatures (T_c) are shifted to a higher temperature with the increase of dopant concentration. This may be due to the crystal polarization, space charge polarization, and temperature-rising ion diffusion [29]. The dielectric constant which decreases above transition temperature may be due to the ferroelectric to a paraelectric phase transition.

It is seen from the tangent loss temperature dependence that the loss raises with an increase in temperature. The rapid increase of the tangent loss in the high-temperature area at low frequencies may be due to the free motion of space charges. The $\tan\delta$ values increase with increase in samarium concentration in the materials (shown in Table 3). This increment in $\tan\delta$ values may be due to the reduction in the domain wall contribution of the ferroelectric and improved electrical conductivity [30].

Variation of polarization and electric field (P-E loop) of unpoled samples $0.5(\text{BiSm}_y\text{Fe}_{1-y}\text{O}_3)-0.5(\text{PbZrO}_3)$ ($y=0.05, 0.10, 0.15, \text{ and } 0.20$) at room temperature is shown in Fig. 4. The nature of loops suggests that the materials are lossy. The study revealed that remanent polarization of the materials is $0.16 \mu\text{C}/\text{cm}^2, 0.14 \mu\text{C}/\text{cm}^2, 0.13 \mu\text{C}/\text{cm}^2, \text{ and } 0.14 \mu\text{C}/\text{cm}^2$ at 12 kV/cm for $0.5(\text{BiSm}_y\text{Fe}_{1-y}\text{O}_3)-0.5(\text{PbZrO}_3)$ ($y=0.05, 0.10, 0.15, \text{ and } 0.20$) respectively. Though a very weak polarization, ferroelectric properties exist in the materials.

Table 2 Comparison of lattice parameters (in \AA) and structural parameters of $0.5(\text{BiSm}_y\text{Fe}_{1-y}\text{O}_3)-0.5(\text{PbZrO}_3)$ ($y=0.05, 0.10, 0.15, 0.20$)

| Materials | a (\AA) | c (\AA) | c/a (\AA) | Crystallite size P (nm) | Dislocation density (δ) (nm^{-2}) | Micro strain (ϵ) | Crystallinity (%) |
|---|--------------------|--------------------|----------------------|---------------------------|---|-----------------------------|-------------------|
| $0.5(\text{BiSm}_{0.05}\text{Fe}_{0.95}\text{O}_3)-0.5(\text{PbZrO}_3)$ | 5.809 | 14.166 | 2.487 | 17 | 0.0034602 | 0.241203 | 64 |
| $0.5(\text{BiSm}_{0.10}\text{Fe}_{0.90}\text{O}_3)-0.5(\text{PbZrO}_3)$ | 5.833 | 14.200 | 2.434 | 18 | 0.0030864 | 0.222293 | 63 |
| $0.5(\text{BiSm}_{0.15}\text{Fe}_{0.85}\text{O}_3)-0.5(\text{PbZrO}_3)$ | 5.811 | 14.195 | 2.442 | 16 | 0.0039062 | 0.261667 | 65 |
| $0.5(\text{BiSm}_{0.20}\text{Fe}_{0.80}\text{O}_3)-0.5(\text{PbZrO}_3)$ | 5.835 | 14.514 | 2.487 | 17 | 0.0034602 | 0.252074 | 61 |

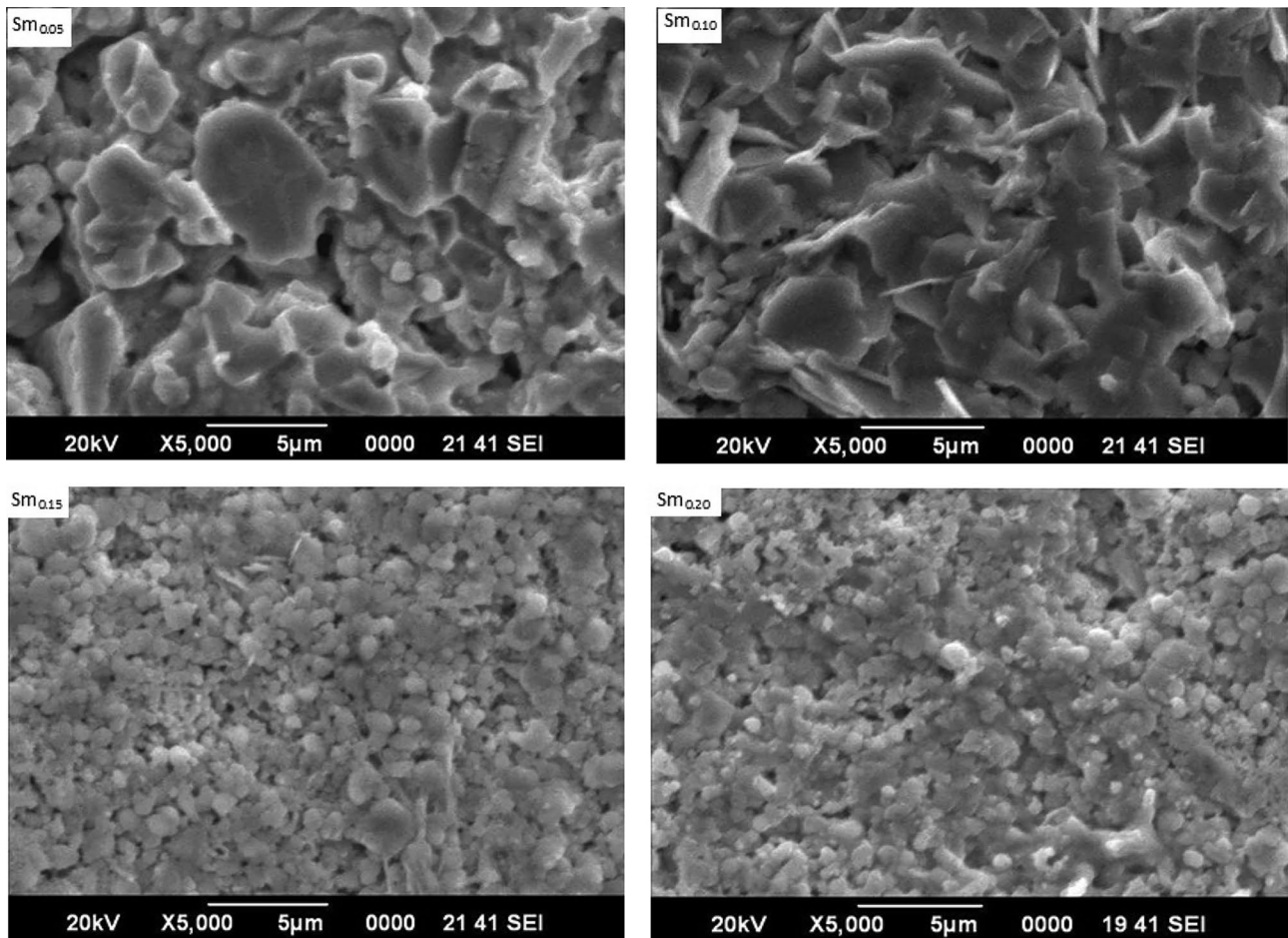


Fig. 2 SEM micrograph of $0.5(\text{BiSm}_y\text{Fe}_{1-y}\text{O}_3)-0.5(\text{PbZrO}_3)$ ($y=0.05, 0.10, 0.15, 0.20$)

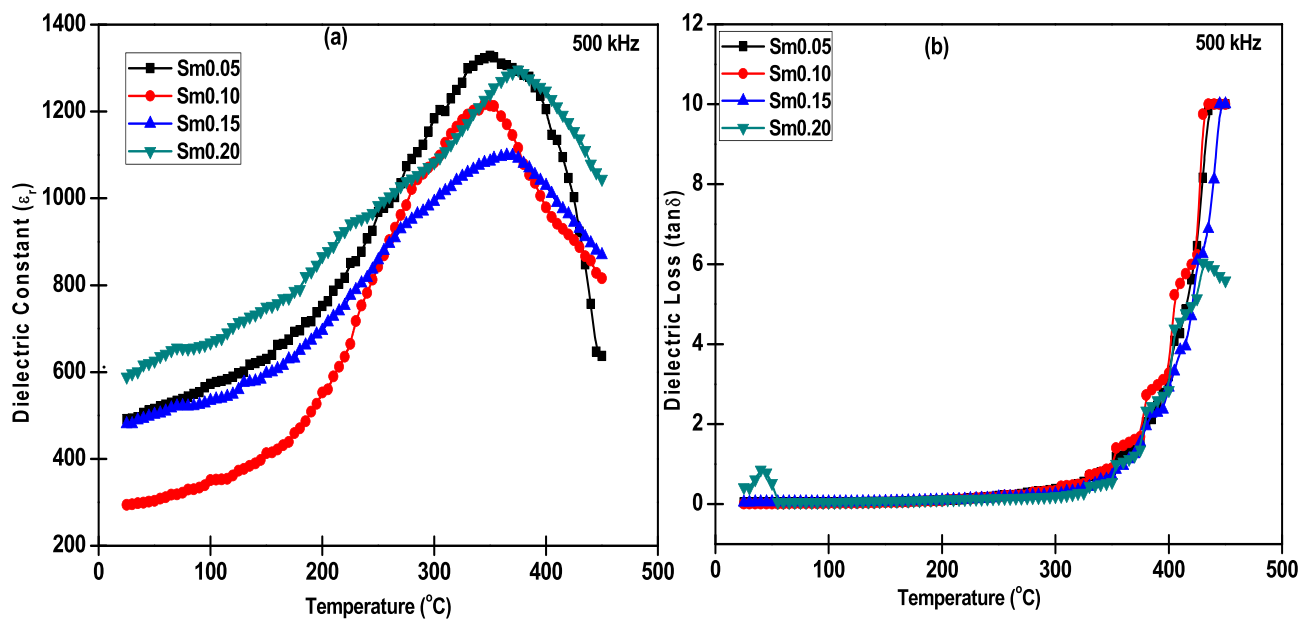


Fig. 3 (a) Variation of dielectric constant (ϵ_r) and (b) dielectric loss ($\tan \delta$) of $0.5(\text{BiSm}_y\text{Fe}_{1-y}\text{O}_3)-0.5(\text{PbZrO}_3)$ ($y=0.05, 0.10, 0.15, 0.20$) with temperature at 500kHz

Table 3 Comparison of dielectric properties and T_c of $0.5(\text{BiSm}_y\text{Fe}_{1-y}\text{O}_3)-0.5(\text{PbZrO}_3)$ ($y=0.05, 0.10, 0.15,$ and 0.20) at 500 kHz

| Materials | ϵ_r at 25 °C | $\tan \delta$ at 25 °C | T_c (°C) | ϵ_r at T_c |
|---|-----------------------|------------------------|------------|-----------------------|
| | 500 kHz | 500 kHz | 500 kHz | 500 kHz |
| $0.5(\text{BiSm}_{0.05}\text{Fe}_{0.95}\text{O}_3)-0.5(\text{PbZrO}_3)$ | 589 | 0.04531 | 360 | 1305 |
| $0.5(\text{BiSm}_{0.10}\text{Fe}_{0.90}\text{O}_3)-0.5(\text{PbZrO}_3)$ | 480 | 0.01173 | 360 | 1154 |
| $0.5(\text{BiSm}_{0.15}\text{Fe}_{0.85}\text{O}_3)-0.5(\text{PbZrO}_3)$ | 294 | 0.04454 | 370 | 1097 |
| $0.5(\text{BiSm}_{0.20}\text{Fe}_{0.80}\text{O}_3)-0.5(\text{PbZrO}_3)$ | 491 | 0.4166 | 370 | 1288 |

3.4 Impedance Study

Impedance spectroscopy is an effective automatic technique that can reveal the relation of electrical properties with the

microstructural properties of the ceramic materials. This technique can be used to separate the contributions of (i) bulk, (ii) grain boundary, and (iii) electrode polarization effects of the material. Electrical ac data of a material can be represented in

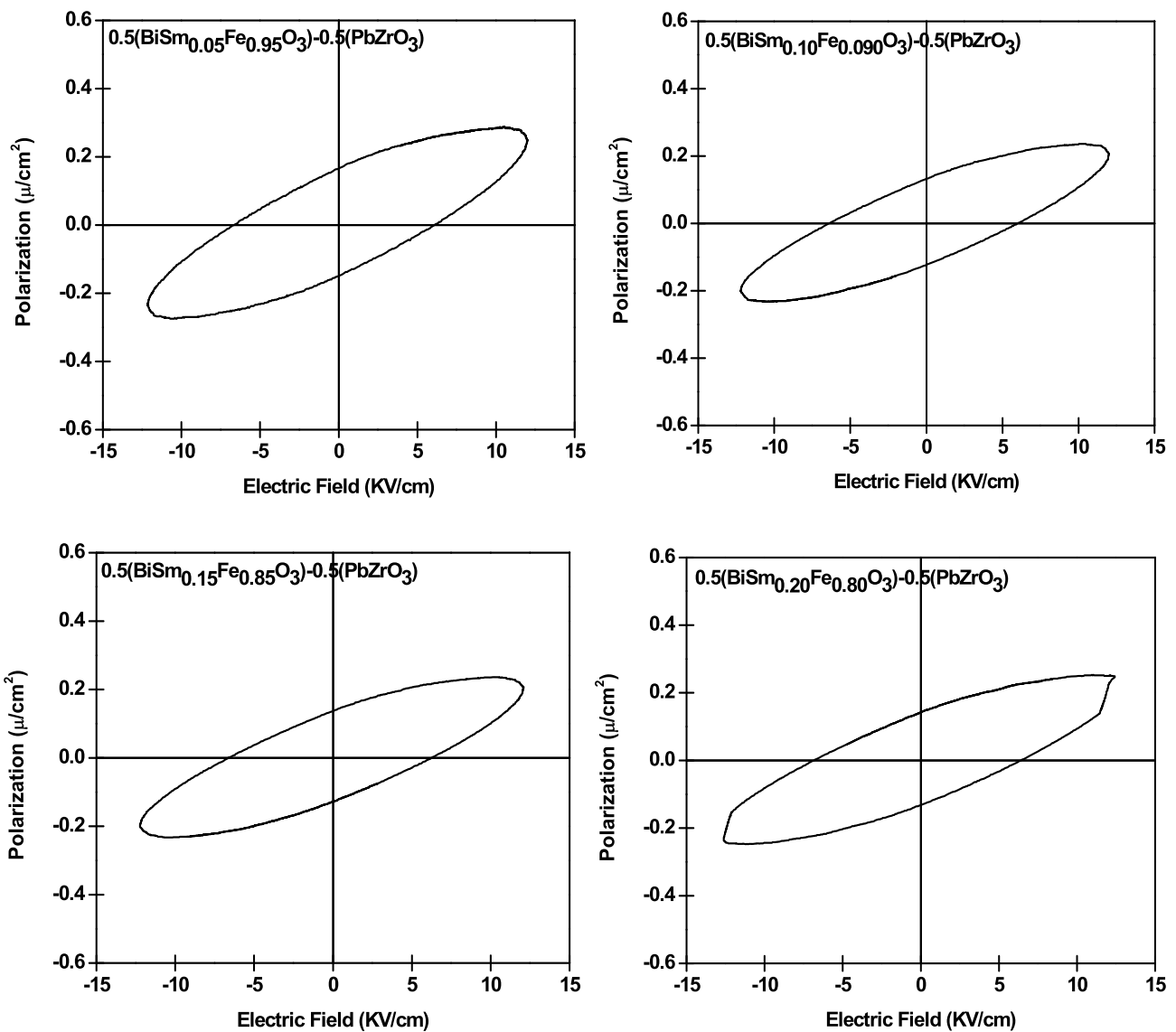


Fig. 4 Variation of polarization and electric field (P-E loop) of unpoled samples $0.5(\text{BiSm}_y\text{Fe}_{1-y}\text{O}_3)-0.5(\text{PbZrO}_3)$ ($y=0.05, 0.10, 0.15,$ and 0.20) at room temperature

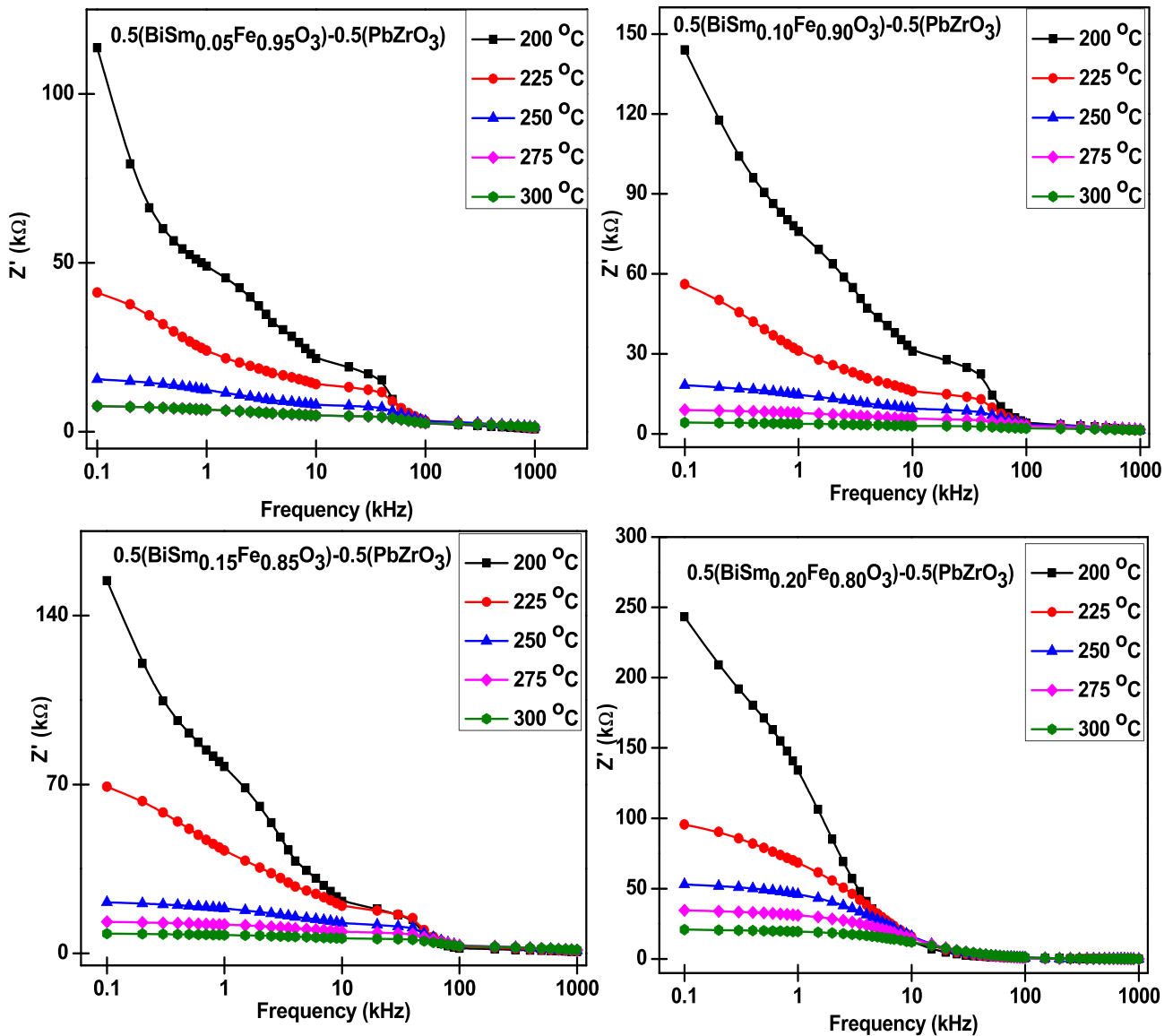


Fig. 5 Variation of Z' as a function of frequency at different temperatures of $0.5(\text{BiSm}_y\text{Fe}_{1-y}\text{O}_3) - 0.5(\text{PbZrO}_3)$ ($y=0.05, 0.10, 0.15,$ and 0.20)

any of the four necessary formalisms [31, 32]: (i) Complex impedance: $Z^*(\omega) = Z'(\omega) - jZ''(\omega)$, where Z' and Z'' are real and imaginary components of impedance, respectively. (ii) Complex admittance: $Y^* = Y' + jY'' = 1/R + j\omega C$. (iii) Complex modulus: $M^* = 1/\epsilon^* = M' + jM'' = j\omega C_0 Z$. (iv) Complex permittivity: $\epsilon^* = \epsilon' - j\epsilon''$. Tangent loss can also be calculated by using the relation, $\tan \delta = \epsilon''/\epsilon' = -Z''/Z' = Y''/Y' = M''/M'$.

Figure 5 shows the variation between real parts of impedance (Z') with frequency at different temperatures. In the low-frequency spectrum, the value of Z' is more significant and obtains a monotonous decline with a rise in frequency.

It may be due to the space charge polarization. The real part of impedance decreases with an increase in temperature and shows a negative temperature coefficient of resistance like semiconductors.

The frequency dependence of imaginary parts of impedance (Z'') is shown in Fig. 6. The figure shows an individual peak for each curve at a specific frequency of about 1 kHz. There is an expanding associated change of these peaks to the more generous frequency side at increasing temperature. The presence of peaks in this plot demonstrates the nature and strength of the electrical relaxation. The expansion of

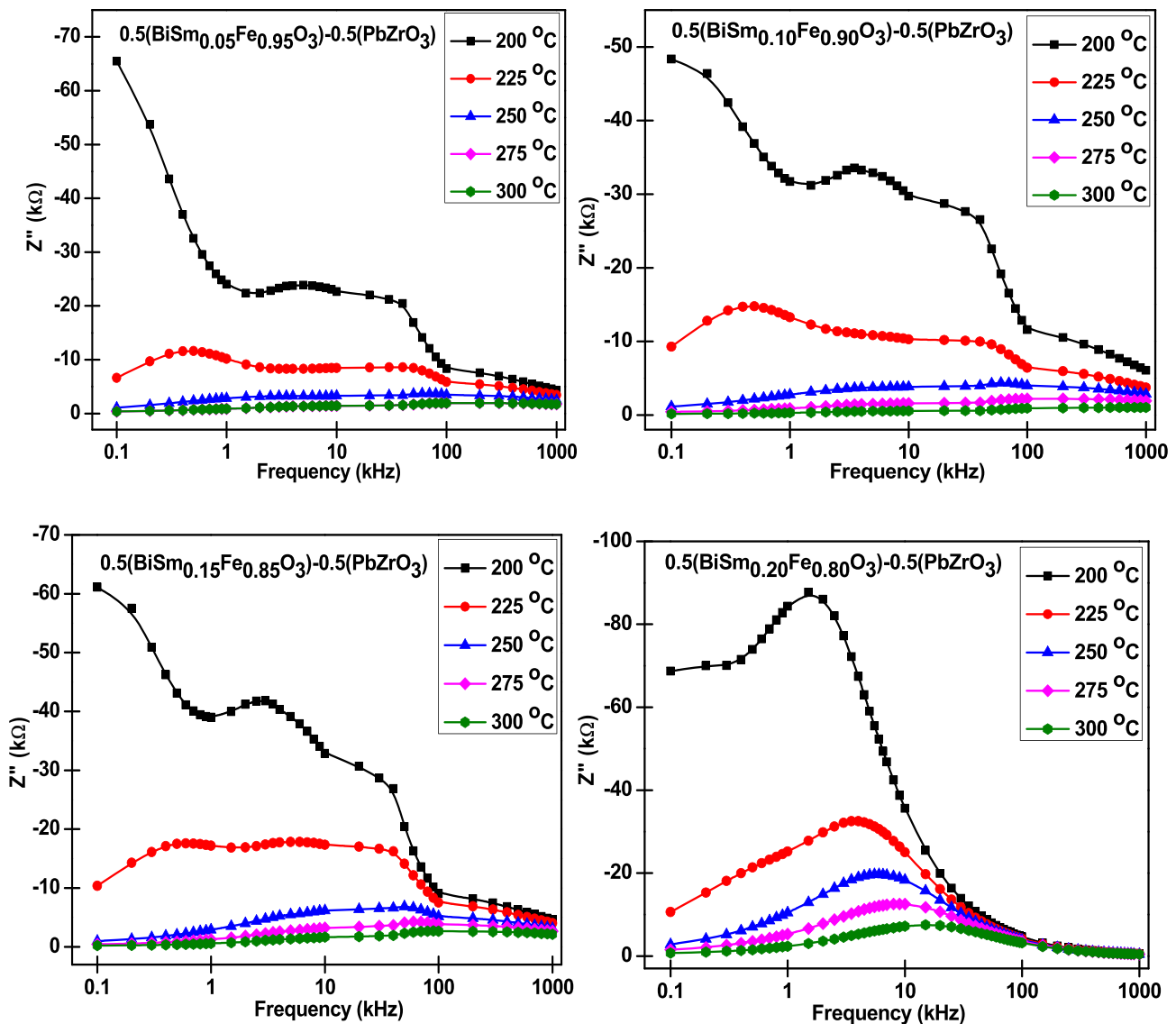


Fig. 6 Variation of Z'' as a function of frequency at different temperatures of $0.5(\text{BiSm}_y\text{Fe}_{1-y}\text{O}_3) - 0.5(\text{PbZrO}_3)$ ($y=0.05, 0.10, 0.15,$ and 0.20)

the asymmetric peak describes the distribution of relaxation time in the material [33]. The first low-frequency peak is associated with the contribution of the grain boundary whereas the second (high frequency) is the bulk response. The peaks are well settled and indicated the grain and interface relaxation phenomena of the corresponding materials [34].

Figure 7 shows the Z' versus Z'' curve. According to Debye's model, a material having a single relaxation time gives rise to ideal semicircles. For the materials, $0.5(\text{BiSm}_{0.05}\text{Fe}_{0.95}\text{O}_3) - 0.5(\text{PbZrO}_3)$, only one semicircle is found indicating a bulk

effect and a slight indication of grain boundary effect. But grain and grain boundary effect for the materials $0.5(\text{BiSm}_{0.15}\text{Fe}_{0.85}\text{O}_3) - 0.5(\text{PbZrO}_3)$ and $0.5(\text{BiSm}_{0.20}\text{Fe}_{0.80}\text{O}_3) - 0.5(\text{PbZrO}_3)$ are clearly identified.

The equivalent circuits (shown in inset of Fig. 7) are excellently fitted with $R(C(R(QR)))$ (CR) for $0.5(\text{BiSm}_{0.05}\text{Fe}_{0.95}\text{O}_3) - 0.5(\text{PbZrO}_3)$ and $0.5(\text{BiSm}_{0.10}\text{Fe}_{0.90}\text{O}_3) - 0.5(\text{PbZrO}_3)$ and $R(C(R(Q(R(C(RW))))))$ for $0.5(\text{BiSm}_{0.15}\text{Fe}_{0.85}\text{O}_3) - 0.5(\text{PbZrO}_3)$ and $0.5(\text{BiSm}_{0.20}\text{Fe}_{0.80}\text{O}_3) - 0.5(\text{PbZrO}_3)$. It is indicated that the simple $R(C(R(QR)))$ (CR) and $R(C(R(Q(R(C(RW))))))$ circuit could show the impedance

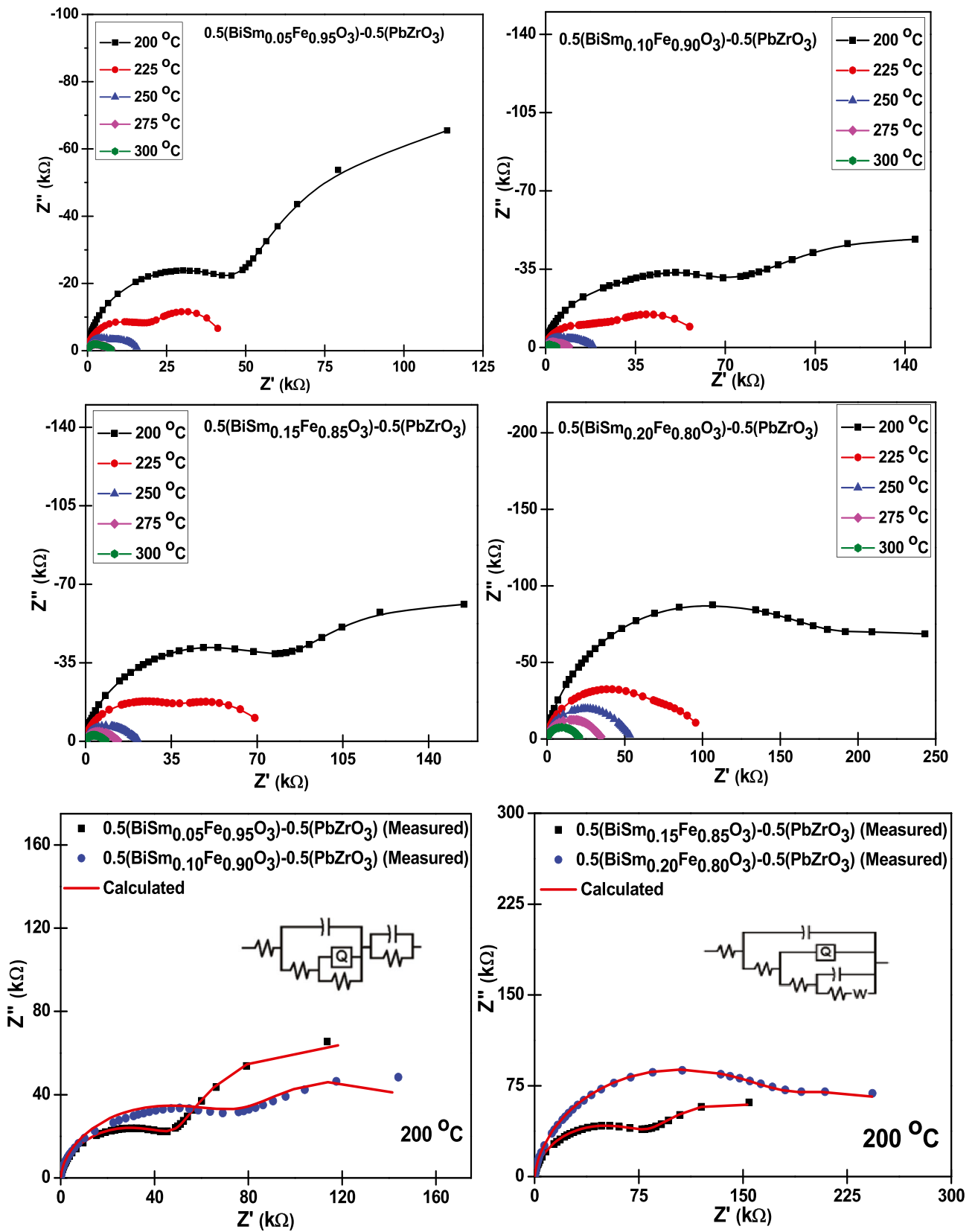


Fig. 7 Complex impedance spectrum (Z' vs. Z'') and fitted impedance data of $0.5(\text{BiSm}_y\text{Fe}_{1-y}\text{O}_3) - 0.5(\text{PbZrO}_3)$ ($y = 0.05, 0.10, 0.15,$ and 0.20) at selected temperatures with equivalent circuits (inset)

Table 4 Values of fitting parameters from equivalent circuits of $0.5(\text{BiSm}_y\text{Fe}_{1-y}\text{O}_3) - 0.5(\text{PbZrO}_3)$ ($y=0.05, 0.10, 0.15,$ and 0.20) at 200°C

| Different parameters | $x = 0.05$ | $x = 0.10$ | $x = 0.15$ | $x = 0.20$ |
|-------------------------|------------------------|------------------------|------------------------|------------------------|
| R_1 | 2.030×10^1 | 5.112×10^1 | 2.507×10^1 | 3.591×10^1 |
| C_1 | 3.85×10^{-10} | 2.71×10^{-10} | 3.48×10^{-10} | 2.94×10^{-10} |
| R_2 | 4.99×10^4 | 6.542×10^3 | 5.726×10^3 | 6.129×10^3 |
| CPE or Q | 1.642×10^{-8} | 6.485×10^{-8} | 6.473×10^{-9} | 2.967×10^{-9} |
| Frequency power (n) | 6.044×10^{-1} | 4.683×10^{-1} | 6.670×10^{-1} | 7.171×10^{-1} |
| R_3 | 4.921×10^4 | 9.168×10^4 | 9.652×10^4 | 2.056×10^5 |
| C_2 | 1.218×10^8 | 1.416×10^{-8} | 9.73×10^{-9} | 1.46×10^{-8} |
| R_4 | 1.233×10^5 | 7.329×10^4 | 9.097×10^4 | 8.308×10^4 |
| W | - | - | 2.473×10^{-6} | 8.647×10^{-6} |
| Chi-square | 1.816×10^{-4} | 2.271×10^{-3} | 1.512×10^{-4} | 1.31×10^{-4} |

data ($\chi^2 \sim 10^{-4}$) and the parameters of each fitting as shown in Table 4.

3.5 Conductivity Study

Figure 8 shows the variation of ac conductivity (σ_{ac}) of $0.5(\text{BiSm}_y\text{Fe}_{1-y}\text{O}_3) - 0.5(\text{PbZrO}_3)$ ($y=0.05, 0.10, 0.15,$ and 0.20) with frequency at different temperatures. There are three regions through which conductivity varies with frequency, i.e., (i) low-dispersion frequency-dependent region, (ii) plateau or frequency-independent region, and (iii) high-frequency-dependent region. The solid lines in the ac conductivity spectra display the similarity of exponential data to the power-law expression: $\sigma_{ac} = \sigma_0 + A\omega^n$ [35], where A is a parameter with the unit of conductivity, n is a dimensionless parameter, and ω is the angular frequency at which the conductivity σ is measured. From the conductivity spectrum, it is evident that the materials systematically show a steadily growing trend towards growing frequency. However, a frequency-independent plateau-like area appears in the low-frequency spectrum as a comparative assessment of conductivity spectra. Consequently, the nature of conductivity rises with a rise in frequency and temperature, indicating that the negative temperature coefficient of resistance is present in the materials. All plots of ac-conductivity tend to fuse at greater frequencies.

It is confirmed that the linear rise in the value of parameter n with temperature between 200 and 300°C may be the reason for the increase of electrode polarization contribution with temperatures for all concentrations. It is noticed that charge carriers take a translational motion with a sudden hopping for $n < 1$, a localized hopping of the species (small hopping without leaving the neighborhood) for $n > 1$, and it behaves like an ideal capacitor for $n = 1$ [36]. n depends on the temperature and decreases with increasing temperature which follows the small polaron model (Table 5).

Depending on the slope and temperature, the spectrum of ac-conductivity is splitted into distinct areas as shown in Fig. 9. The value of ac conductivity rises in the low-temperature region and very low in the high-temperature zone. For all the materials, the activation energies are determined in the temperature regions 25 – 220°C and 225 – 450°C . The activation energies (E_a) are minimal for all the materials at low-temperature and high-temperature regions as shown in Table 6. The graph shows thermally activated process in the materials.

3.6 Magnetic Study

The magnetic properties of $0.5(\text{BiSm}_y\text{Fe}_{1-y}\text{O}_3) - 0.5(\text{PbZrO}_3)$ ($y=0.05, 0.10, 0.15,$ and 0.20) have been studied from magnetization vs. magnetic field intensity (hysteresis loop) with a maximum applied field of 15 kG as shown in Fig. 10. The remanent magnetization (M_r) of the materials is found to be 0.011 emu/gm , 0.74 emu/gm , 0.14 emu/gm , and 0.005 emu/gm for $0.5(\text{BiSm}_y\text{Fe}_{1-y}\text{O}_3) - 0.5(\text{PbZrO}_3)$ ($y=0.05, 0.10, 0.15,$ and 0.20) respectively. This indicates that remanent magnetization decreases with an increase in concentration. Antiferromagnetic behavior is observed in the $0.5(\text{BiSm}_y\text{Fe}_{1-y}\text{O}_3) - 0.5(\text{PbZrO}_3)$ ($y=0.05, 0.10, 0.15,$ and 0.20) ceramics.

3.7 Thermistor Properties

3.7.1 Electrical Resistance

The electrical resistance of $0.5(\text{BiSm}_y\text{Fe}_{1-y}\text{O}_3) - 0.5(\text{PbZrO}_3)$ ($y=0.05, 0.10, 0.15,$ and 0.20) is determined from the impedance data. The variation of resistance with temperatures (ranging from 175 to 350°C) is decreasing exponentially which confirmed the NTCR behavior [37] of materials as shown in Fig. 11(a). It is observed that the materials become more electrically conductive with the decrease in the concentration of dopant Samarium.

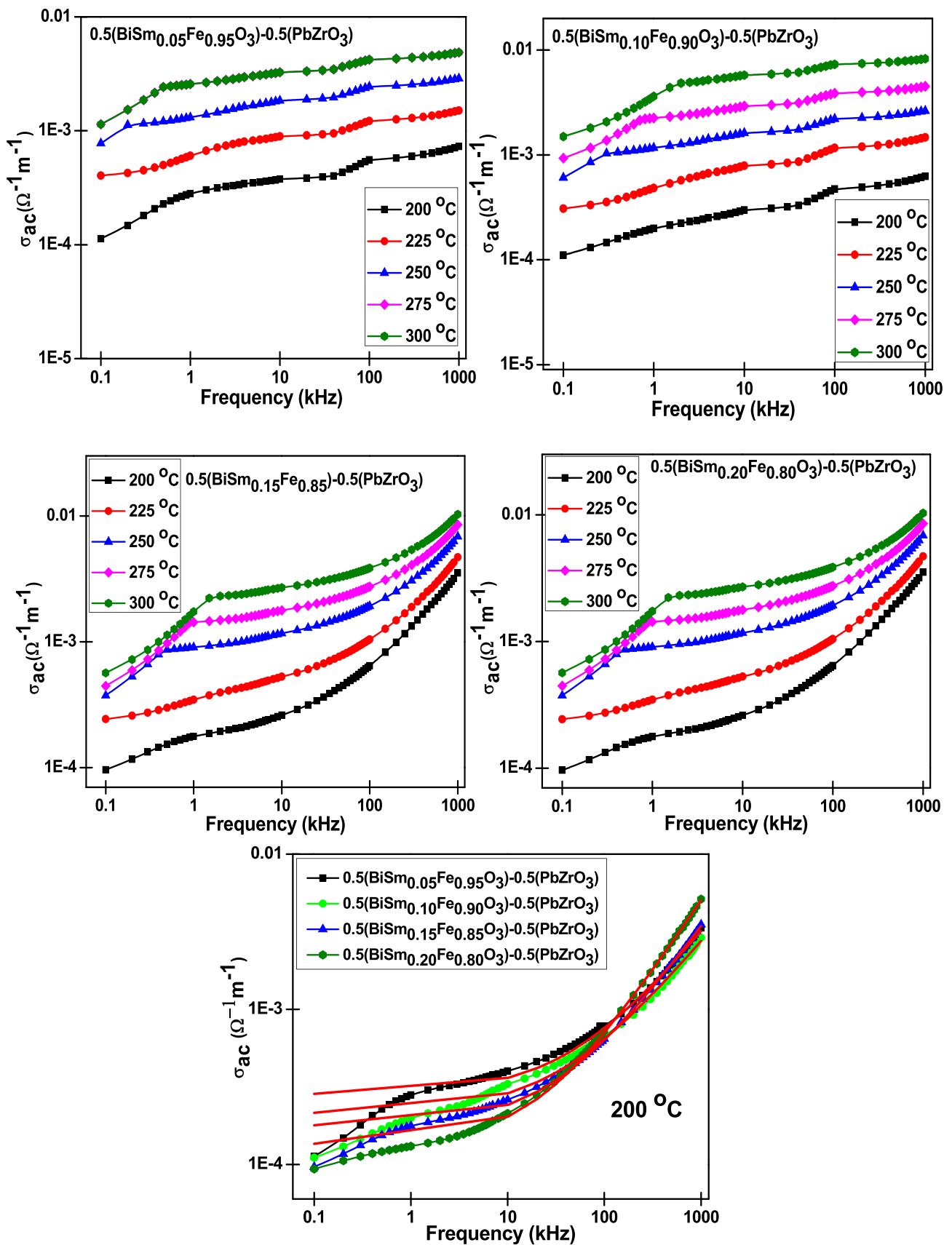


Fig. 8 Variation of ac conductivity (σ_{ac}) with frequency of $0.5(BiSm_yFe_{1-y}O_3) - 0.5(PbZrO_3)$ ($y = 0.05, 0.10, 0.15,$ and 0.20) at different temperatures

Table 5 Fitting parameters obtained from the Johnson power law at 200 °C

| Composition | 0.5BiSm _{0.05} Fe _{0.95} O ₃ -0.5PbZrO ₃ 200 °C | 0.5BiSm _{0.10} Fe _{0.90} O ₃ -0.5PbZrO ₃ 200 °C | 0.5BiSm _{0.15} Fe _{0.85} O ₃ -0.5PbZrO ₃ 200 °C | 0.5BiSm _{0.20} Fe _{0.80} O ₃ -0.5PbZrO ₃ 200 °C |
|--|---|---|---|---|
| σ_{dc} ($\Omega^{-1} m^{-1}$) | 2.8312×10^{-4} | 2.12957×10^{-4} | 1.77642×10^{-4} | 1.35216×10^{-4} |
| A | 5.5716×10^{-8} | 6.19356×10^{-8} | 2.50746×10^{-8} | 1.27202×10^{-8} |
| n | 0.78621 | 0.76893 | 0.85231 | 0.93106 |

Electrical resistance (R) of Negative Temperature Coefficient (NTC) thermistors can be explained as a function of temperature which is related by the equation $\ln(R_T) = \frac{1}{T} + C$, where R_T represents the resistance of the sample at respective temperature T .

From Fig. 11(b), the linear behavior of materials explained the excellent NTCR characteristics as reported [38]. The deviation in graphs for some materials is because of systematic errors in processing parameters, the effect of sintering, and doping contents.

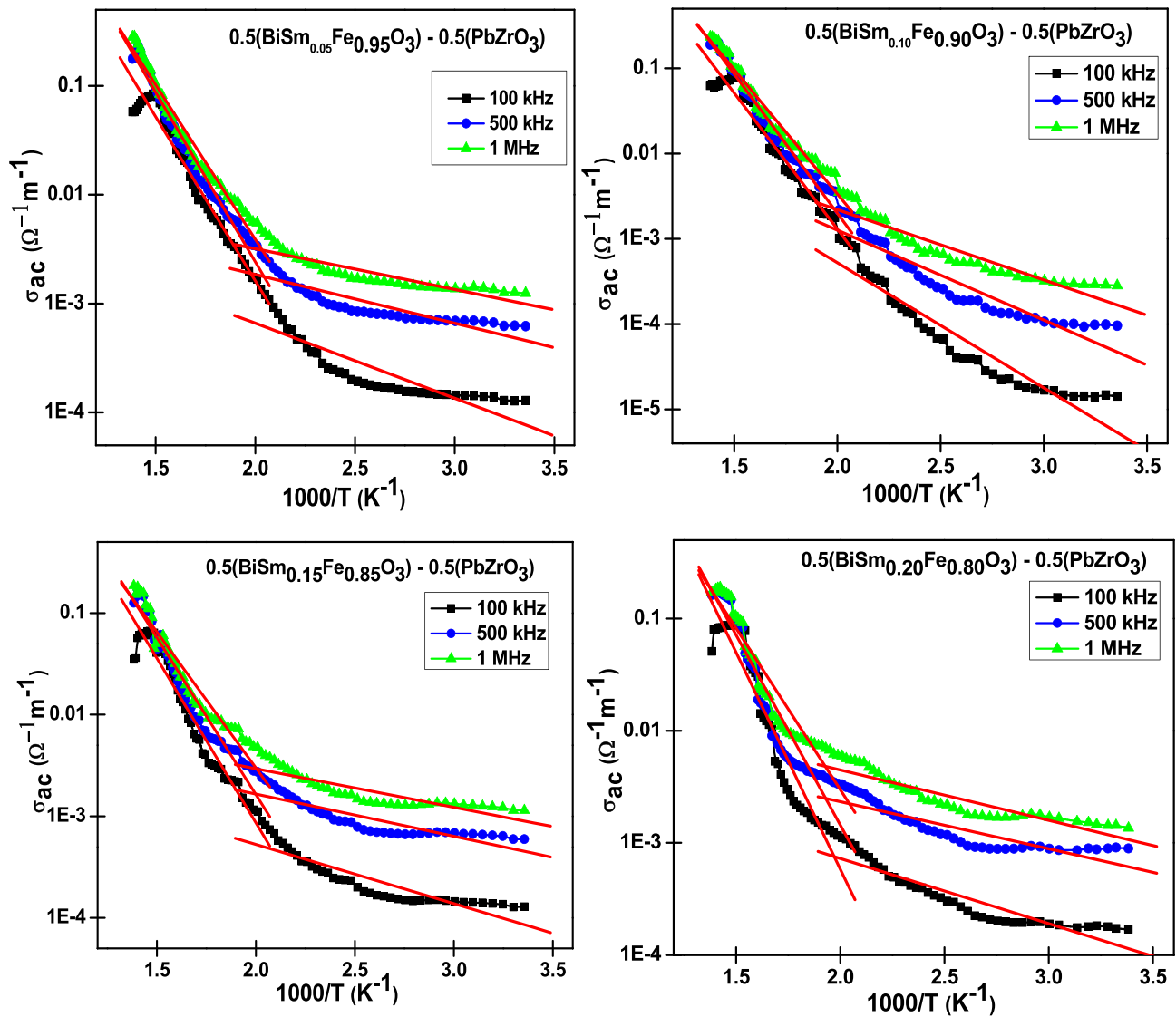


Fig. 9 Variation of ac conductivity (σ_{ac}) with $(1000/T)$ of $0.5(\text{BiSm}_y\text{Fe}_{1-y}\text{O}_3) - 0.5(\text{PbZrO}_3)$ ($y=0.05, 0.10, 0.15,$ and 0.20) at 100 kHz, 500 kHz, and 1 MHz

Table 6 Values of activation energies (eV) of $0.5(\text{BiSm}_y\text{Fe}_{1-y}\text{O}_3) - 0.5(\text{PbZrO}_3)$ ($y=0.05, 0.10, 0.15,$ and 0.20) at 100 kHz for different temperature range

| Materials | Frequency (kHz) | 25–220 °C E_a (eV) | 225–450 °C E_a (eV) |
|---|-----------------|-------------------------|--------------------------|
| $0.5(\text{BiSm}_{0.05}\text{Fe}_{0.95}\text{O}_3) - 0.5(\text{PbZrO}_3)$ | 100 | 0.1366 | 0.5984 |
| | 500 | 0.0887 | 0.6176 |
| | 1000 | 0.0740 | 0.5642 |
| $0.5(\text{BiSm}_{0.10}\text{Fe}_{0.90}\text{O}_3) - 0.5(\text{PbZrO}_3)$ | 100 | 0.2908 | 0.6335 |
| | 500 | 0.2091 | 0.6474 |
| | 1000 | 0.1636 | 0.5793 |
| $0.5(\text{BiSm}_{0.15}\text{Fe}_{0.85}\text{O}_3) - 0.5(\text{PbZrO}_3)$ | 100 | 0.1157 | 0.6427 |
| | 500 | 0.0826 | 0.6123 |
| | 1000 | 0.0753 | 0.5300 |
| $0.5(\text{BiSm}_{0.20}\text{Fe}_{0.80}\text{O}_3) - 0.5(\text{PbZrO}_3)$ | 100 | 0.1152 | 0.7668 |
| | 500 | 0.0831 | 0.6722 |
| | 1000 | 0.0888 | 0.5702 |

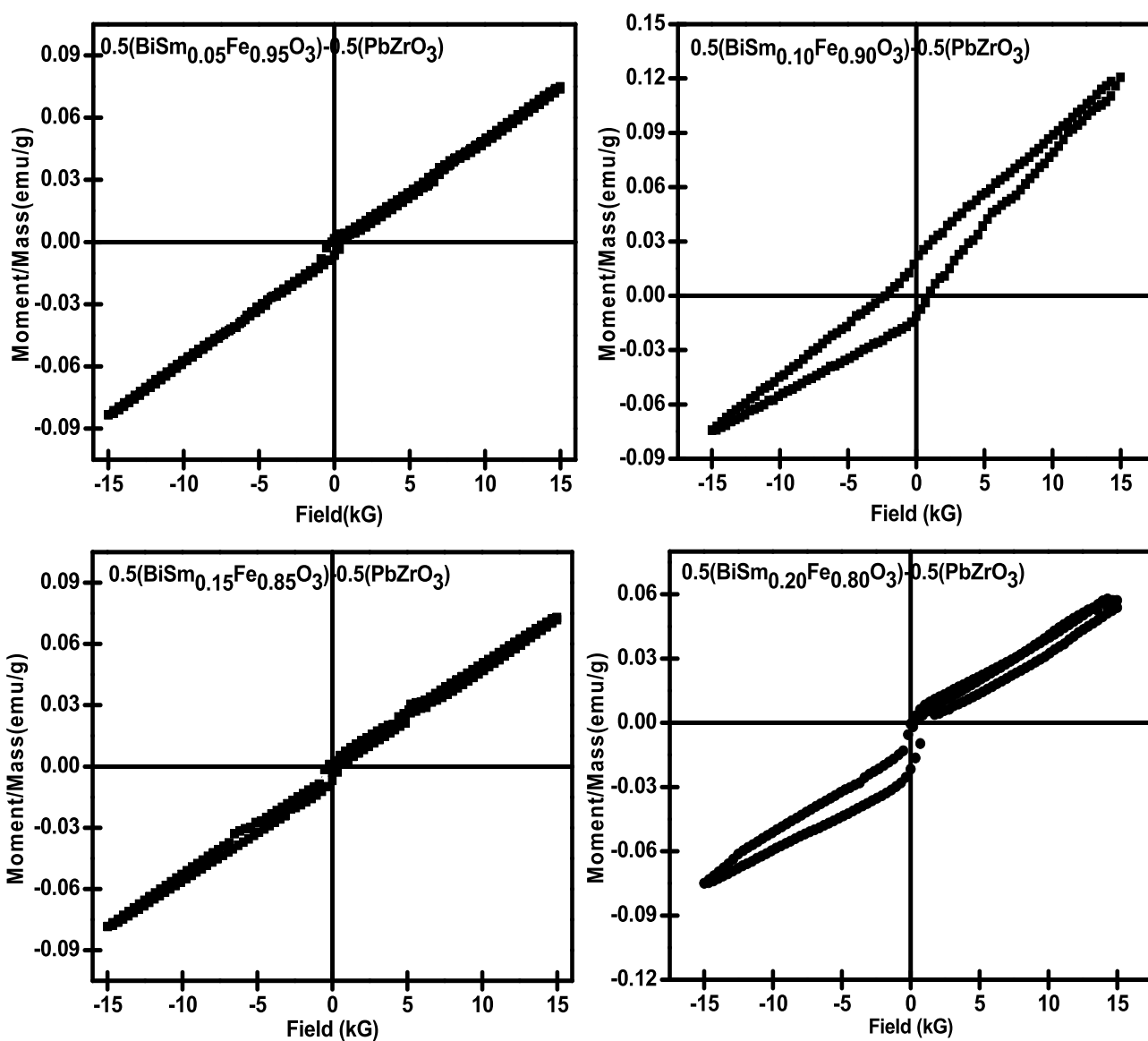


Fig. 10 Magnetic hysteresis loops of $0.5(\text{BiSm}_y\text{Fe}_{1-y}\text{O}_3) - 0.5(\text{PbZrO}_3)$ ($y=0.05, 0.10, 0.15,$ and 0.20) at room temperature

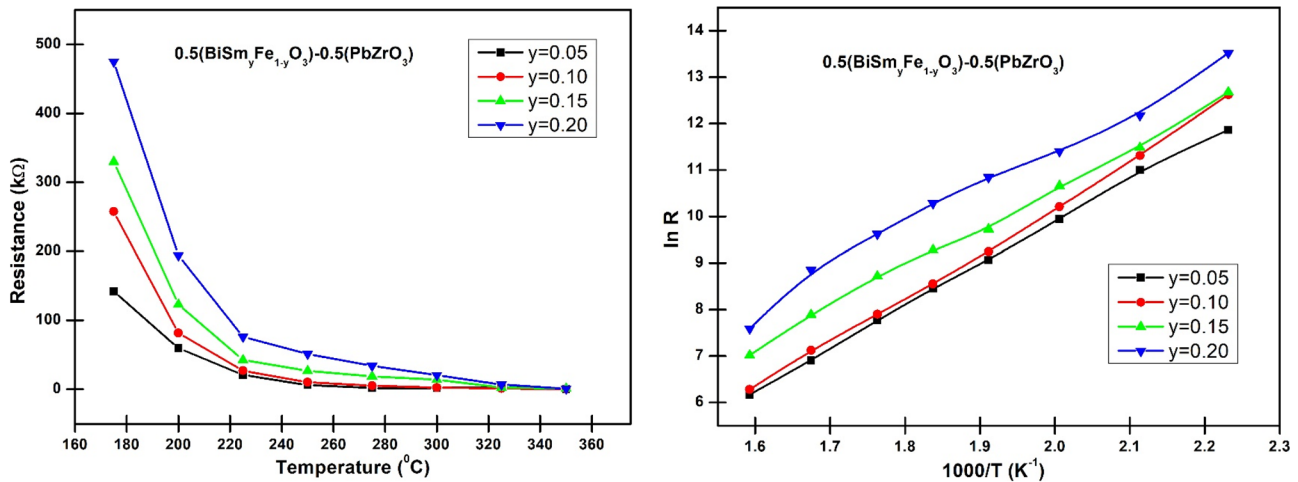


Fig. 11 (a) Variation of Resistance (R) with temperature (T) and (b) variation of logarithmic resistance ($\ln R$) with inverse temperature ($1000/T$) of $0.5(\text{BiSm}_y\text{Fe}_{1-y}\text{O}_3)-0.5(\text{PbZrO}_3)$ ($y=0.05, 0.10, 0.15, 0.20$)

3.7.2 Thermistor constant (β)

The thermistor constant β values of all the compositions at different temperatures are calculated using the relation $\beta = \ln\left(\frac{R_1}{R_2}\right) / \left(\frac{1}{T_1} - \frac{1}{T_2}\right)$ in the temperature range of 175–350 $^{\circ}\text{C}$.

β values of all the materials at different temperatures are observed between 4289 and 6584K which are higher than the available NTC thermistors [39] in the market and industry. The activation energy of the materials is calculated using the relation [40] $E_a = K_B\beta$, where K_B represents Boltzmann constant. These are in the range of industrial NTC thermistors for temperature sensing.

It is observed that the material $0.5\text{BiSm}_{0.20}\text{Fe}_{0.80}\text{O}_3-0.5\text{PbZrO}_3$ is more adequate for thermistor fabrication due to the high value of thermistor constant, and activation energy than others. As the values of the thermistor constant increases with rise in temperature and doping concentration as mentioned in Table 7, it can be applicable for medical

applications, thermistor-based devices, temperature sensors, etc. [41, 42].

3.7.3 Sensitivity

The value of sensitivity index or temperature coefficient of resistance (α) is an important parameter for the characterization of the thermistor. This can be determined from the value of thermistor constant β using the relation of Steinhart–Hart coefficient $\beta = \sqrt{\left(\frac{b}{3c}\right)^3 + \frac{a^2}{4}}$ [43, 44] which can be simplified as $\alpha = \frac{a-T}{c} = \frac{-\beta}{T^2}$. The sensitivity index (α) is generally described in percentage per Kelvin (%/K) [45, 46]. For a good thermistor, the sensitivity index should fall between -1 and -9% which is approximately equal to experimental data as mentioned in Table 7. It is also confirmed that α decreases with rise in thermistor constant β . Some variations of sensitivity may be due to the existence of extrinsic charge carriers in grain.

Table 7 Temperature-dependent thermistors constant (β), activation energy (E_a), and sensitivity index (α) of $0.5\text{BiSm}_y\text{Fe}_{1-y}\text{O}_3-0.5\text{PbZrO}_3$ ($y=0.05, 0.10, 0.15, 0.20$)

| Temperature ($^{\circ}\text{C}$) | $0.5\text{BiSm}_{0.05}\text{Fe}_{0.95}\text{O}_3-0.5\text{PbZrO}_3$ | | | $0.5\text{BiSm}_{0.10}\text{Fe}_{0.90}\text{O}_3-0.5\text{PbZrO}_3$ | | | $0.5\text{BiSm}_{0.15}\text{Fe}_{0.85}\text{O}_3-0.5\text{PbZrO}_3$ | | | $0.5\text{BiSm}_{0.20}\text{Fe}_{0.80}\text{O}_3-0.5\text{PbZrO}_3$ | | |
|------------------------------------|---|---------|----------|---|---------|----------|---|---------|----------|---|---------|----------|
| | β | E_a | α | β | E_a | α | β | E_a | α | β | E_a | α |
| 175 | 4289.1831 | 0.36961 | -2.136 | 4438.2696 | 0.38246 | -2.21 | 4818.5619 | 0.41523 | -2.399 | 5095.64083 | 0.43911 | -2.537 |
| 200 | 4580.7911 | 0.39474 | -2.046 | 4941.4871 | 0.42582 | -2.207 | 5285.6327 | 0.45548 | -2.361 | 5536.37544 | 0.47709 | -2.473 |
| 225 | 4997.5335 | 0.43065 | -2.014 | 5366.1194 | 0.46241 | -2.162 | 5682.8572 | 0.48971 | -2.29 | 5913.63077 | 0.5096 | -2.383 |
| 250 | 5511.6100 | 0.47495 | -2.014 | 5681.1712 | 0.48956 | -2.076 | 5977.1269 | 0.51507 | -2.184 | 6192.75869 | 0.53365 | -2.263 |
| 275 | 6046.2013 | 0.52102 | -2.012 | 5861.1805 | 0.50508 | -1.951 | 6142.6514 | 0.52933 | -2.044 | 6347.72969 | 0.547 | -2.113 |
| 300 | 5764.3232 | 0.49673 | -1.755 | 5997.051 | 0.51678 | -1.826 | 6265.3995 | 0.53991 | -1.907 | 6460.91687 | 0.55676 | -1.967 |
| 325 | 5091.1547 | 0.43872 | -1.423 | 6144.9440 | 0.52953 | -1.718 | 6399.1607 | 0.55143 | -1.789 | 6584.3816 | 0.5674 | -1.84 |

Based on the above explanation, it is confirmed that all the materials are suitable for NTC thermistors with better performance and thermistor constant as well as low sensitivity as shown in Table 7.

4 Conclusions

$0.5(\text{BiSm}_y\text{Fe}_{1-y}\text{O}_3)-0.5(\text{PbZrO}_3)$ ($y=0.05, 0.10, 0.15,$ and 0.20) materials are synthesized through solid-state reaction technique. Rhombohedral structure is confirmed for all the materials. The average value of the crystallite size is found to be in the range of 16–18 nm. It is observed that the average grain sizes are within the range of 5 μm , demonstrating that the grains are bigger than the average crystallite size. The material transition temperature is found to be 360 °C and 370 °C. The remanent polarization of materials is found to be 0.16 $\mu\text{C}/\text{cm}^2$, 0.14 $\mu\text{C}/\text{cm}^2$, 0.13 $\mu\text{C}/\text{cm}^2$, and 0.14 $\mu\text{C}/\text{cm}^2$ for $0.5(\text{BiSm}_{0.05}\text{Fe}_{0.95}\text{O}_3)-0.5(\text{PbZrO}_3)$, $0.5(\text{BiSm}_{0.10}\text{Fe}_{0.90}\text{O}_3)-0.5(\text{PbZrO}_3)$, $0.5(\text{BiSm}_{0.15}\text{Fe}_{0.85}\text{O}_3)-0.5(\text{PbZrO}_3)$, and $0.5(\text{BiSm}_{0.20}\text{Fe}_{0.80}\text{O}_3)-0.5(\text{PbZrO}_3)$ respectively suggesting a very weak polarization. The Nyquist plot reveals the contribution of bulk and grain boundary effect of the materials. The ac conductivity varies as a power law of the form $\sigma_{ac} = \sigma_0 + A\omega^n$, with n is found to be in the range 0.76–0.93 at 200 °C. The materials show antiferromagnetic behavior at higher concentrations. The α value lies between -1 and -9% which is suitable material for NTC thermistors with better performance. The studied materials can be useful for thermistor-based device and temperature sensor application because of the high value of β , i.e., greater than 4000 K.

Declarations

Conflict of Interest The authors declare no competing interests.

References

- H.Y. Dai, Z.P. Chen, T. Li, R.Z. Xue, J. Chen, Structural and electrical properties of bismuth ferrite ceramics sintered in different atmospheres. *J. Supercond. Nov. Magn.* **26**(10), 3125–3132 (2013). <https://doi.org/10.1007/s10948-013-2130-7>
- D.C. Jia, J.H. Xu, H. Ke, W. Wang, Y. Zhou, Structure and multiferric properties of BiFeO_3 powders. *J. Eur. Ceram. Soc.* **29**(14), 3099–3103 (2009). <https://doi.org/10.1016/j.jeurceramsoc.2009.04.023>
- A. Srinivas, D.-W. Kim, K.S. Hong, Significant changes in the ferroelectric properties of BiFeO_3 modified $\text{SrBi}_2\text{Ta}_2\text{O}_9$. *Appl. Phys. Lett.* **83**, 1602 (2003)
- I. Coondoo, A.K. Jha, Enhancement of ferroelectric and piezoelectric characteristics in europium substituted $\text{SrBi}_2\text{Ta}_2\text{O}_9$ ferroelectric ceramics. *Mater. Lett.* **63**(1), 48–50 (2009)
- Q.Y. Shao, A.D. Li, Y.F. Tang, H.Q. Ling, N.B. Ming, Influence of doping and buffer layers on $\text{Pb}(\text{Zr}, \text{Ti})\text{O}_3$ thin films derived from inorganic zirconium precursor. *Mater. Chem. Phys.* **75**(1–3), 207–210 (2002)
- G.H. Lin, R. Fu, S. He, J. Sun, X. Zhang, L. Sengupta, Reliability and stability of novel tunable thin film. *MRS Online Proc. Lib. (OPL)*. **720** (2002)
- C.M. Krowne, S.W. Kirchoefer, W. Chang, J.M. Pond, L.M.B. Alldredge, Examination of the possibility of negative capacitance using ferroelectric materials in solid state electronic devices. *Nano Lett.* **11**(3), 988–992 (2011)
- T. Gao, Z. Chen, Q. Huang, F. Niu, X. Huang, L. Qin, Y. Huang, A review: preparation of bismuth ferrite nanoparticles and its applications in visible-light induced photocatalyses. *Rev. Adv. Mater. Sci.* **40**(2), 97–109 (2015)
- M.D. Casper, M.D. Losego, J.P. Maria, Optimizing phase and microstructure of chemical solution-deposited bismuth ferrite (BiFeO_3) thin films to reduce DC leakage. *J. Mater. Sci.* **48**(4), 1578–1584 (2013)
- G.S. Lotey, N.K. Verma, Magnetodielectric properties of rare earth metal-doped BiFeO_3 nanoparticles. *J. Mater. Sci.: Mater. Electron.* **24**(10), 3723–3729 (2013)
- H.C. Wang, Y.H. Lin, Y.N. Feng, Y. Shen, Photocatalytic behaviors observed in Ba and Mn doped BiFeO_3 nanofibers. *J. Electroceramics* **31**(1–2), 271–274 (2013)
- O.P. Bajpai, J.B. Kamdi, M. Selvakumar, S. Ram, D. Khastgir, S. Chattopadhyay, Effect of surface modification of BiFeO_3 on the dielectric, ferroelectric, magneto-dielectric properties of polyvinylacetate/ BiFeO_3 nanocomposites. *EXPRESS Polym. Lett.* **8**(9), 669–681 (2014)
- H.B. Sharma, K.N. Devi, V. Gupta, J.H. Lee, S.B. Singh, Ac electrical conductivity and magnetic properties of $\text{BiFeO}_3-\text{CoFe}_2\text{O}_4$ nanocomposites. *J. Alloys Compd.* **599**, 32–39 (2014)
- P. Suresh, P.D. Babu, S. Srinath, Role of (La, Gd) co-doping on the enhanced dielectric and magnetic properties of BiFeO_3 ceramics. *Ceram. Int.* **42**(3), 4176–4184 (2016)
- S. Madolappa, S. Kundu, R. Bhimireddi, K.B.R. Varma, Improved electrical characteristics of Pr-doped BiFeO_3 ceramics prepared by sol-gel route. *Mater. Res. Express* **3**(6), 065009 (2016)
- P. Kumar, C. Panda, M. Kar, Effect of rhombohedral to orthorhombic transition on magnetic and dielectric properties of La and Ti co-substituted BiFeO_3 . *Smart Mater. Struct.* **24**(4), 045028 (2015)
- R. Das, G.G. Khan, S. Varma, G.D. Mukherjee, K. Mandal, Effect of quantum confinement on optical and magnetic properties of Pr-Cr-codoped bismuth ferrite nanowires. *J. Phys. Chem. C* **117**(39), 20209–20216 (2013)
- V.V. Jadhav, R.S. Mane, P.V. Shinde, Electrochemical super capacitors of bismuth ferrites. in *Bismuth-Ferrite-Based Electrochemical Supercapacitors*. (Springer, Cham., 2020), pp. 69–84
- C. Anthonyraj, M. Muneeswaran, S.G. Raj, N.V. Giridharan, V. Sivakumar, G. Senguttuvan, Effect of samarium doping on the structural, optical and magnetic properties of sol-gel processed BiFeO_3 thin films. *J. Mater. Sci.: Mater. Electron.* **26**(1), 49–58 (2015)
- K.S. Nalwa, A. Garg, A. Upadhyaya, Effect of samarium doping on the properties of solid-state synthesized multiferric bismuth ferrite. *Mater. Lett.* **62**(6–7), 878–881 (2008)
- C.S. Tu, C.S. Chen, P.Y. Chen, H.H. Wei, V.H. Schmidt, C.Y. Lin, ... J.M. Lee, Enhanced photovoltaic effects in A-site samarium doped BiFeO_3 ceramics: the roles of domain structure and electronic state. *J. Eur. Ceram. Soc.* **36**(5), 1149–1157 (2016)
- H. Liu, Universal dielectric relaxation induced giant dielectric permittivity in Mn-doped PbZrO_3 ceramics. *Ceram. Int.* **45**(8), 10380–10384 (2019)
- A. Ray, B. Behera, T. Basu, S. Vajandar, S.K. Satpathy, P. Nayak, Modification of structural and dielectric properties of

- polycrystalline Gd-doped BFO–PZO. *J. Adv. Dielectr.* **8**(05), 1850031 (2018)
24. S.K. Satpathy, S. Sen, B. Behera, Dielectric, electrical and magnetic properties of La doped BiFeO₃–PbZrO₃ composites. *J. Mater. Sci.: Mater. Electron.* **28**(12), 9102–9113 (2017)
 25. S.K. Satpathy, N.K. Mohanty, A.K. Behera, S. Sen, B. Behera, P. Nayak, Dielectric and electrical properties of BiFeO₃–PbZrO₃ composites. *J. Electron. Mater.* **44**(11), 4290–4299 (2015)
 26. S.K. Satpathy, N.K. Mohanty, A.K. Behera, B. Behera, P. Nayak, Electrical conductivity of Gd doped BiFeO₃–PbZrO₃ composite. *Front. Mater. Sci.* **7**(3), 295–301 (2013)
 27. S.K. Satpathy, N.K. Mohanty, A.K. Behera, B. Behera, Dielectric and electrical properties of 0.5(BiGd_{0.05}Fe_{0.95}O₃)-0.5(PbZrO₃), composite. *Mater. Sci. -Pol.* **32**(1), 59–65 (2014)
 28. P. Scherrer, Bestimmung der inneren Struktur und der Größe von Kolloidteilchen mittels Röntgenstrahlen. In *Kolloidchemie Ein Lehrbuch.* (Springer, Berlin, Heidelberg, 1912), pp. 387–409
 29. S.A. Ivanov, P. Nordblad, R. Tellgren, T. Ericsson, S.K. Korchagina, L.F. Rybakova, A. Hewat, Influence of PbZrO₃ doping on the structural and magnetic properties of BiFeO₃. *Solid State Sci.* **10**(12), 1875–1885 (2008)
 30. B. Dhanalakshmi, P. Kollu, B.P. Rao, P.S. Rao, Impedance spectroscopy and dielectric properties of multiferroic BiFeO₃/Bi_{0.95}Mn_{0.05}FeO₃–Ni_{0.5}Zn_{0.5}Fe₂O₄ composites. *Ceram. Int.* **42**(2), 2186–2197 (2016)
 31. I.M. Hodge, M.D. Ingram, A.R. West, Impedance and modulus spectroscopy of polycrystalline solid electrolytes. *J. Electroanal. Chem.* **74**(2), 125–143 (1976)
 32. A. Lahmar, S. Habouti, C.H. Solterbeck, M. Es-Souni, B. Elouadi, Correlation between structure, dielectric, and ferroelectric properties in BiFeO₃–LaMnO₃ solid solution thin films. *J. Appl. Phys.* **105**(1), 014111 (2009)
 33. K. Auromun, S. Hajra, R.N.P. Choudhary, B. Behera, Structural, dielectric and electrical characteristics of yttrium modified 0.7 BiFeO₃–0.3 PbTiO₃. *Solid State Sci.* **101**, 106139 (2020)
 34. S. Hajra, M. Sahu, V. Purohit, R.N.P. Choudhary, Dielectric, conductivity and ferroelectric properties of lead-free electronic ceramic: 0.6 Bi(Fe_{0.98}Ga_{0.02})O₃–0.4 BaTiO₃. *Heliyon* **5**(5), e01654 (2019)
 35. H. Mahamoud, B. Louati, F. Hlel, K. Guidara, Conductivity and dielectric studies on (Na_{0.4}Ag_{0.6})₂PbP₂O₇ compound. *Bull. Mater. Sci.* **34**(5), 1069–1075 (2011)
 36. J.R. Macdonald, Comparison of the universal dynamic response power-law fitting model for conducting systems with superior alternative models. *Solid State Ion.* **133**(1–2), 79–97 (2000)
 37. S. Sahoo, S.K.S. Parashar, S.M. Ali, CaTiO₃ nano ceramic for NTCR thermistor-based sensor application. *J. Adv. Ceram.* **3**(2), 117–124 (2014)
 38. E.A. de Vasconcelos, S.A. Khan, W.Y. Zhang, H. Uchida, T. Katsube, Highly sensitive thermistors based on high-purity polycrystalline cubic silicon carbide. *Sens. Actuator A Phys.* **83**(1–3), 167–171 (2000)
 39. R.M. Mahani, D.A. Aziz, A thermistor with variable rate of negative temperature coefficient of resistance made from Egyptian raw materials. *J. Electron. Mater.* **49**(12), 7443–7447 (2020)
 40. A.K. Sahu, P. Mallick, S.K. Satpathy, B. Behera, Effect on structural, electrical and temperature sensing behavior of neodymium doped bismuth ferrite. *Adv. Mater. Lett.* **12**(7), 21071648 (2021)
 41. C. Yuan, X. Liu, M. Liang, C. Zhou, H. Wang, Electrical properties of Sr–Bi–Mn–Fe–O thick-film NTC thermistors prepared by screen printing. *Sens. Actuator A Phys.* **167**(2), 291–296 (2011)
 42. P. Mallick, A.K. Sahu, S.K. Biswal, Investigation on structural, dielectric, thermistor parameters and negative temperature coefficient behaviour of Nd, Gd, and La-doped bismuth ferrite. *Trans. Electr. Electron. Mater.* 1–13 (2022)
 43. R.N. Jadhav, S.N. Mathad, V. Puri, Studies on the properties of Ni_{0.6}Cu_{0.4}Mn₂O₄ NTC ceramic due to Fe doping. *Ceram. Int.* **38**(6), 5181–5188 (2012)
 44. J. Kulawik, D. Szwegierczak, B. Gröger, A. Skwarek, Fabrication and characterization of bulk and thick film perovskite NTC thermistors. *Microelectron. Int.* (2007)
 45. S. Sahoo, Enhanced time response and temperature sensing behavior of thermistor using Zn-doped CaTiO₃ nanoparticles. *J. Adv. Ceram.* **7**(2), 2 (2018)
 46. X. Xiong, J. Xu, P. Zhao, L. Wang, L. Bian, F. Xu, ... A. Chang, Structural and electrical properties of thick film thermistors based on perovskite La–Mn–Al–O. *Ceram. Int.* **40**(7), 10505–10510 (2014)

Publisher's Note Springer Nature remains neutral with regard to jurisdictional claims in published maps and institutional affiliations.

Springer Nature or its licensor holds exclusive rights to this article under a publishing agreement with the author(s) or other rightsholder(s); author self-archiving of the accepted manuscript version of this article is solely governed by the terms of such publishing agreement and applicable law.